Tunable Schottky Barriers in Ultrathin Black Phosphorus Field Effect Transistors *via* Polymer Capping

Yanyong Li, Shenghuang Lin, Yanghui Liu, Yang Chai and Shu Ping Lau[*]

Dr. Y. Y. Li,[⊥] Dr. S. H. Lin,[⊥] Dr. Y. H. Liu, Dr. Y. Chai, Prof. S. P. Lau

Department of Applied Physics, the Hong Kong Polytechnic University, Hung Hom, Kowloon, Hong Kong, P. R. China

E-mail: apsplau@polyu.edu.hk

[⊥] These authors contributed equally.

Keywords: ultrathin black phosphorus, ambipolar field effect transistor, PMMA capping, Schottky barrier

[*] E-mail: apsplau@polyu.edu.hk

Abstract

It is still a great challenge to avoid the degradation of ultrathin black phosphorus (BP) since its discovery in 2014. Various methods have been explored to stabilize the properties of ultrathin BP through capping technology or chemical passivation. Besides, the large metal-semiconductor contact resistance is also one of the critical issues. The two problems hinder the further development of ultrathin BP devices. Herein, we demonstrate that polymethyl methacrylate (PMMA) capping can not only enhance the durability of the ultrathin BP effectively and nondestructively, but also tune the effective Schottky barriers (SBs) formed at the interfaces between the metal and semiconductor dramatically. Particularly, the Schottky barrier (SB) for electron injection from metal to semiconductor is decreased by ~ 13 meV and the performance of the BP field effect transistor (FET) is strongly enhanced with the current on/off ratio increased by 6.8 times for the hole conduction after the PMMA capping. In addition, after the electron beam irradiation to the PMMA layer, the charge neutral point of the BP FET exhibits remarkable negative shift resulting in the electron dominated semiconductor channel at zero gate voltage. Furthermore, through partially capping the BP channel, a prototype of BP p-n diode was demonstrated with a maximum rectification factor of 21.3. The diode performs quite well with just a quarter of the BP channel capped by the PMMA layer. Our findings suggest that the PMMA capped ultrathin BP would be a promising choice for future device applications.

1.Introduction

The surge of black phosphorus (BP) research promotes the innovation of two-dimensional (2D) materials family and its applications. BP is a layered semiconductor consisting of puckered phosphorus atom planes with strong intralayer covalent bonds and weak van der Waals interlayer interaction. Compared with the representative 2D materials, such as graphene and transition metal dichalcogenides (TMDs), BP owns both intrinsic thickness dependent bandgap ranging from ~0.3 eV in bulk to ~2.0 eV in monolayer and favorable field effect mobility (~1000 $cm^2/V{\cdot}s$) at room temperature.[1-4] In addition to these advantages above, the puckered honeycomb structure leads to highly anisotropic electrical transport, thermal conductivity, optical responses and mechanical elastic moduli.[5-9] Hence, BP is regarded as a promising candidate for future high-performance logic circuit, optoelectronics, energy storage and molecular sensors.[10-14] However, the weak ambient stability is the Achilles' Heel, nanoscale BP suffers from the degradation in ambient environment within several hours primarily due to the reaction with oxygen.[15-20] Thus, finding a proper way of protecting ultrathin BP against degradation is imperative and full of challenge. Up to now, the problem can be surmounted by various capping schemes including Al_2O_3[21-23], SiO_2[24], hexagonal boron nitride (h-BN) or graphene sandwich structure[25-27], polymer[28, 29] or by different chemical decoration, including titanium sulfonate ligand[30], aryl diazonium moieties[31], and benzyl viologen[32]. Among these methods, atomic layer deposition (ALD) introduces excess water in the growth process of Al_2O_3, which is not suitable for ultrathin BP. The encapsulation of sandwiched h-BN or graphene is normally used to assemble heterostructure and has a low throughput. Various chemicals decoration may be toxic and unstable for a durable protection. Capping polymer is regarded as one of the most promising methods. Polymethyl methacrylate (PMMA) is a kind of common non-hazardous organic material. It can be used to encapsulate ultrathin BP flake. Tayari *et al* utilized

PMMA to protect BP quantum wells.[28] However, the effect of PMMA on the intrinsic properties of ultrathin BP has not been studied in details.

Only the ultrathin BP with proper and durable protection should be competent for various electronic, photonic and energy storage applications. Field effect transistor (FET) as a basic three-terminal device constitutes the contemporary microelectronic industry. However, BP MOSFETs suffer from high contact resistance due to the Schottky barriers (SBs) formed at the metal-semiconductor interfaces. Unlike traditional silicon based FETs, 2D materials are difficult to form heavily doped regions effectively by ion implantation.[33-35] The contact resistance is highly dependent on the Fermi level alignment of the source/drain electrodes with the semiconductor energy bands.[36, 37] There are two main approaches for tuning the SBs at the interface by choosing the metal electrode with appropriate work function and surface electrostatic doping.[38, 39] High work function metals, such as Ni and Pd, have been demonstrated to achieve different SB heights and the alignment of Fermi levels close to the valance band (E_V) facilitating hole injection. Likewise, low work function metal, such as Sc, boosts the electron injection and gives a record high current density of 580 μA/μm in BP Schottky barrier-MOSFET (SB-MOSFET).[40, 41] Though choosing a proper metal is able to modify the SBs effectively, the Fermi level pinning can make the metal's Fermi level pinned at a fixed energy level, which hinders the optimization of this tuning method. Recently, surface electrostatic doping method inspires researchers to alter the work function of BP and energy level alignment by the aid of various adsorbates, such as metal atoms,[42, 43] silicon nitride,[44] caesium carbonate and molybdenum trioxide,[45] benzyl viologen,[32, 46] aluminum oxide,[47] ary diazonium,[31] potassium,[48] various polymers[49] and so on. Furthermore, the method of gate electrostatic doping is also used to create p-n diodes of few-layer BP.[50, 51] However, combing the requirement of durable protection and SB adjustment for ultrathin BP devices together, PMMA capping is considered as one of the most

appropriate methods to satisfy both requirements simultaneously. Therefore, it is critical to fully understand the influence of PMMA capping on the SB adjustment in BP SB-MOSFETs.

In this study, we investigate the electrical transport properties of the PMMA capped BP MOSFETs by analyzing the current-voltage (I-V) characteristics quantitatively. The shapes of the I-V curves are very much affected by the height and width of the effective SBs.[52] Through adjusting the effective SBs, the conduction type of BP MOSFET can be varied from holes to electrons at zero gate voltage. The effective SB for electron injection is decreased remarkably after the capping. Moreover, the performance of the BP MOSFET is also enhanced substantially with higher on/off ratios. Finally, the prototypes of p-n diode and logic inverter based on ultrathin BP were also demonstrated successfully *via* e-beam irradiation to the PMMA film partially.[49]

2. Results and discussion

Figure 1(a) shows the Raman spectra of the PMMA capped BP flake as a function of storage time and kept in the ambient environment. Three characteristic peaks A_g^1, B_{2g} and A_g^2 are located at 362 cm^{-1}, 439 cm^{-1} and 467 cm^{-1}, respectively, which are in good agreement with the reported results.[53, 54] After 17 hours of storage, no obvious Raman peak shifts were observed for the three Raman modes. The intensity ratio of the three peaks maintained at about 1:1.1:2.0 in the whole period. The unchanged Raman spectra suggest that the PMMA capping can protect the BP flake from degradation effectively. In addition, it is known that the degradation can reduce the field effect mobilities by an order of magnitude.[19, 55, 56] Hence, a standard BP MOSFET was fabricated to investigate the protective effect of the PMMA layer. The field effect mobility μ_{FE} can be extracted from the linear region of the FET transfer curves. Based on the formula, $\mu_{FE} = L/W \cdot (1/C_g) \cdot (dG/dV_g)$, where L and W are the length and width of the FET channel, respectively, C_g is the capacitance per unit area, V_g is

the gate voltage and the *G* is the conductance. The hole mobilities and electron mobilities at different preserving time stages were calculated as shown in Figure 1(b). It is found that both the hole and electron mobilities of the PMMA capped FET are almost unchanged up to 50 hours. The inset shows the atomic force microscope (AFM) image of the BP sample revealing a clean surface without any bubbles. The thickness of the ultrathin BP flake is ~9.8 nm. It is worth mentioning that the AFM measurements were carried out after removing the PMMA layer and all the following FETs were fabricated based on flakes with the thickness less than 10 nm.

The capping PMMA layer can not only make the devices durable but also change the effective SBs. Unlike the silicon MOSFETs, the electrical transport properties of BP FETs are highly dependent on the metal-semiconductor contacts due to the considerable SBs at the interfaces. To investigate the PMMA capping effect on the electrical transport properties, we measured the I-V characteristics of the capped FETs as compared with the uncapped ones, which directly reflect the properties of the effective SBs.[52, 57] All experiments were carried out at room temperature and in a vacuum ambient (10^{-6} Torr). The linear and semi-logarithmic plots of the transfer curves are shown in Figure 2(a). Herein, an obvious ambipolar behavior is observed with asymmetric hole and electron branches, which is attributed to the small band gap of the ultrathin BP and a weak Fermi level pinning at the Cr/BP interfaces.[14] The red curves derive from the capped device. The drain current of the BP FET decreases gradually and then followed by a shallow increase as the V_g becomes more positive with a minimum current at ~ +30 V. Whereas, the minima of the uncapped device is located at +57 V (black curve). In this article, we define the gate voltage at minimum drain current as the charge neutral point.[58] The clear shift of the charge neutral point suggests that the PMMA capping dramatically modulates the effective SBs by the surface electrostatic n-type doping.[59] The prominent p-type behavior in the uncapped FET indicates that the Fermi level of the Cr aligns with the energy level of

the BP near the E_v, which facilitates the hole injection into the channel. The energy bands of BP bend upward to form two triangular SBs, namely, the source and drain barriers.[58, 60] After the capping, the PMMA layer induces positive fixed charges at the interface.[42, 45, 47] In order to preserve charge neutrality, the fixed positive charges must be balanced by an equal amount of charges with opposite sign in the BP. This charge transfer results in dipoles over a distance of atomic dimensions, which causes the strong downward band bending of BP and even forms an inversion layer.[61-63] The strong downward band bending inevitably reduces the depletion width of the triangular SBs formed at the interface between the contact edge and BP.[64, 65] The change of the SBs will facilitate the electron injection into the BP channel, *i.e.* reduces the effective SBs for electrons. Figure 2(b) shows the schematic diagrams of the energy bands under the influence of the PMMA capping. In the flat-band condition, the Fermi level of the Cr electrode aligns close to the E_v of the BP as shown in the upper panel of Figure 2(b). Notably, the conduction band minimum in the bulk is equal to that at the interface, and the activation energy is same as the SBs in flat-band condition.[66] So, flat-band voltage (V_{FB}) is a key point, where the thermionic emission region is separated with tunneling region.[67] Assuming the FET is in the flat-band condition, $q\Phi_{Bn}$ and $q\Phi_{Bp}$ represent the effective SBs for electron and hole injection, respectively. Obviously, the $q\Phi_{Bn}$ is much larger than $q\Phi_{Bp}$, which means the hole conductance dominates the MOSFET in this case. By contrast, after capping the PMMA layer, the effective SBs for electron to decrease, but for hole to increase as shown in the lower panel of Figure 2(b).[63] Besides of the negative shift of charge neutral point, it is found that the off-state drain current also declines obviously after the capping. Herein, we define the on-state current as the value of the drain current at V_g = -70 V and V_d = 100 mV and the off-state current is the value of the drain current at the charge neutral point. It is known that the off-state current density highly depends on the changes of the effective SBs.[67] Low off-state current contributes proportionally to increasement of the

on/off ratio in the SB-MOSFET. Obviously, the off-state current in the capped device decreases by about ten times, from 1.3×10^{-8} A to 1.7×10^{-9} A. Accordingly, the on/off current ratio is found to be ~ 7.5×10^{3} for the hole conduction, which is much larger than that in the uncapped device (~ 1.1×10^{3}). Due to the ultrathin channel thickness and improved electrostatic control, the V_g dramatically influences the width of the source and drain SBs, which is known as the gate electrostatic doping effect.[68] Figure 2(c) displays the I-V characteristics of the SB-MOSFET under various gate voltages. The slopes of the I-V curves increase gradually as the V_g become more negative, which reflects the increase of conductivity in the hole dominated side. For instance, as the V_g varies from 30 V to -20 V gradually, the conductivity of the uncapped device rises from 3.75 S/m (V_g= 30 V) to 33.5 S/m (V_g= -20 V). In contrast, the outcomes in the capped device are significantly distinct. As shown in Figure 2(d), though the I-V curves are still symmetric and linear in the hole side (V_g < 20 V), the conductivity of the FET decreases a little to 31 S/m at the same V_g = -20 V, which indicates that the hole conduction is suppressed after the capping. The variation of the total resistance of the FET may derive from the change of the effective SBs at the contacts and/or the n-type doped BP channel. Given only the latter one is taken into account, the shape of the I-V curve should maintain symmetry and linearity. However, in the inset of Figure 2(d), the I-V curves in the capped FET become asymmetric and rectified as the V_g becomes positive (from 20 V to 30 V). Therefore, the change of the SBs at the contacts should play an important role in the variation of the total resistance. As discussed above, the PMMA capping causes strong downward band bending of the BP, which inevitably leads to the change of the contact resistance.[69] As for the question, how do the SBs at the source and drain contacts change? The model of back-to-back SB diodes can be employed for the explanation.[52] In this model, the source and drain SBs lie in reverse and forward states, respectively. Besides of the V_g, the drain bias (V_d) also affects the effective SBs dramatically. In the experiments,

V_d was the same (100 mV) for the capped and uncapped FETs in the condition of V_g = +30 V. Surprisingly, the shapes of the I-V curves are distinct obviously. The capped FET has already lain in the electron dominated side, when the V_g reaches +30 V, which indicates that the PMMA capping readily promotes the drain SB to reach the flat-band condition in the capped FET. As the drain SB in the MOSFET lies in the forward state, the combination of V_g and V_d determines the shape of the drain SB. Through narrowing the width of the triangular drain SB, the mechanism of electron injection is the tunneling or thermionic field emission, which decreases the effective SB for electron injection remarkably. So, the difference between the source and drain SBs leads to the asymmetry of the I-V curves in the same conditions for the capped and uncapped FETs. Furthermore, with the help of the additional downward band bending induced by the PMMA capping, it is easier for the electron injection from the drain to be dominated by tunneling or thermionic field emission in the same V_g and V_d in the capped FET. Hence, it should be easier to observe the asymmetric I-V curves in the electron dominated side in the capped FET. Since the negative shift of the charge neutral point reflects the degree of the additional downward band bending, to ascertain the capping effect, more FETs (11 devices) were measured to verify the shifts of the charge neutral points. Clear negative shifts of the charge neutral points were observed in all these devices with the maximum shift magnitudes of -38 V. The details can be found in the part 2 of the supplementary information.

To further evaluate the PMMA capping influence, we have to extract the effective SBs using flat-band SB extraction method.[70] Notably, we indicate that the flat-band voltage (V_{FB}) is denoted as the point in the subthreshold regime where the slope of the semi-logarithmic I_d versus V_g deviating from linear trend.[50] Note that the V_{FB} divides the whole transfer curve in the off-state into two regions, the hole tunneling region dominated by carrier tunneling possibility and thermionic emission region.[71] Below the V_{FB}, hole tunneling current is hindered effectively due to the substantial SB

width. So, the contribution from the hole tunneling current can be neglected in the off-state. By contrast, the hole thermionic emission current is limited by the channel potential V_d below V_{FB} following the classic thermionic emission (TE) theory, and the SB height above the V_{FB}. When the MOSFET reaches flat-band condition, the total activation energy that holes must overcome to access the channel is equal to the effective SB for hole. Hence, the effective SB can be revealed once the V_{FB} is identified.

Figure 3(a) displays the transfer curves of another uncapped BP FET under different temperatures. Herein, the drain current I_d is composed of both the thermionic emission current and tunneling current. To simplify the calculation, we use the conventional TE theory to simulate the drain current in the high temperature range. Using the conventional TE equation,

$$J_d = A^* T^2 \exp(\frac{-q\Phi_B}{k_B T})[\exp(\frac{qV_d}{k_B T}) - 1]$$

we used the Arrhenius-type plot, *i.e.* -ln (I_d/T^2) *vs* the reciprocal of the temperature ($1/k_BT$), to extract the effective SB as shown in Figure 3(b). Herein, J_d is the drain current density through the FET, A^* is the Richardson's constant, k_B is the Boltzmann constant, T is the temperature, $q\Phi_B$ is the effective SB and V_d is the drain bias. Through extracting the slopes of the curves in Figure 3(b) in the high temperature region, the effective SBs at different V_g were obtained. Then, the V_{FB} can be readily determined from the curve of $q\Phi_B$ as a function of the V_g as shown in Figure 3(c). In the off-state, only the thermionic current determines the current flow through the device. V_{FB} is reached when the tunneling current becomes relevant in the total current flow, which is reflected by the fact that the calculated $q\Phi_B$ deviates from the linear trend.[72] Hence, the extracted effective SB for hole at V_{FB} is about 44.6 meV in the uncapped device. Notably, negative effective SBs were calculated when the V_g was less than 7 V. It may result from the contact-limited effects and ultrathin-body induced thermal

assisted tunneling.[72, 73] Referring to the band gap of ~10 nm BP of ~290 meV, the corresponding effective SB for electron is about 245.4 meV.[4, 50, 74] After the PMMA capping, the effective SB for hole conduction can be calculated by the same method as shown in Figure 3(d). The value is about 57.6 meV for $q\Phi_{Bp}$ and 232.4 meV for $q\Phi_{Bn}$. Therefore, the effective SB for electron injection is decreased by ~ 13 meV after the PMMA capping.

It is reported that electron beam (e-beam) irradiation can solidify PMMA film by cross-linking and create small molecular free radicals to introduce positive fixed charges at the interfaces between BP and PMMA.[49, 75] Hence, we also employed this method to irradiate the PMMA capping layer for comprehensive understanding the influence of PMMA capping. Another BP MOSFET was fabricated in the same processes. The schematic diagram of the irradiation process is displayed in Figure 4(a). A layer of PMMA was spin-coated onto the as-fabricated FET. After the standard soft baking, e-beam was utilized to expose the PMMA in a specific area, as shown in the step 2 in Figure 4(a). The e-beam irradiated PMMA was solidified and could not be removed by acetone. Next, the unexposed PMMA was rinsed away by acetone. Finally, the FET capped by the irradiated PMMA was fabricated as shown in step 3. The photo of the irradiated BP MOSFET is also shown in Figure 4(a). The details of the irradiation process are described in the methods.

Figure 4(b) displays the transfer characteristics of the BP FET before and after the e-beam irradiation. The V_d was set as 100 mV. After the irradiation, it is found that the ambipolar characteristic of the BP SB-MOSFET is more obvious with a larger drain current (I_d) in the electron dominated side, which is more dramatic than the circumstance described in Figure 2(a). More importantly, the charge neutral point exhibits a substantial negative shift after irradiation, even below $V_g = 0$ V (from +16 V to -6 V). The negative charge neutral point implies that the device is under the control of electrons, when there is no applied gate voltage. It is reported that the positive fixed charges exist at the interfaces between

the irradiated PMMA layer and the BP surface.[49] Hence, masses of electrons induced by the surface electrostatic doping accumulate in the semiconductor channel leading to the negative shift of the charge neutral point. Moreover, these surface charges also enlarge the hysteresis loop formed in the process of forward and backward sweeping the gate voltage. As illustrated in the part 1 of the supplementary information, the hysteresis loop is enlarged after the irradiation implying the increase of the surface charges.

Subsequently, we discuss the influence of the e-beam irradiation on the effective SBs with the reference to I-V curves and band diagrams at different stages. Figures 4(c) shows the I-V curves of the uncapped BP FET in the hole dominated side before irradiation. In the uncapped FET, the Fermi level (E_F) of Cr aligns close to the valence band (E_v) facilitating the hole injection. Negative V_g promotes the hole electrostatic doping making the energy levels bend upward seriously and the top of the E_v gets closer to the E_F as shown in the corresponding band diagram in Figure 5(a). Accordingly, the intrinsic heavy p-type doping results in a shorter depletion width and sizable hole tunneling current, which is revealed by the perfect linear I-V relationship under various gate voltages. The inset of Figure 4(c) shows the enlarged I-V characteristics under different V_g (from -30 V to 10 V), where the V_d ranges from -3 V to 0 V. Interestingly, the I-V curves always maintain the linear relationship without drain current saturation, even when the V_d increases as large as to -3 V. This behavior reveals that the effective SB for hole is too small to affect the device output. It is known that the saturation behavior in 2D FETs is not attributed to the pinch-off of the inversion layer in conventional Si MOFET, but to the current limitation of the source and drain SBs.[41] As we mentioned before, the V_d can also modify the effective SB near the drain side. With the increasing V_d, the drain SB becomes more and more smaller, which is expected to have less impact on the output curve. Therefore, the I_d-V_d curves in the enlarged range display perfect linear without saturation.

In contrast, the I-V curves of the SB-MOSFET in the hole side are obviously distinct after the irradiation as shown in Figure 4(d). The I-V curves deviate from the linear relationship, which means that the effective SB for hole ($q\Phi_{Bp^*}$) increases as explained above. The intrinsic hole transport in the irradiated FET is suppressed, like the circumstance in the capped FET without irradiation described in Figure 2(d). The energy bands of the BP are dragged down to form larger triangular SB as shown in Figure 5(b), which impedes the hole injection, especially the tunneling current. The increased effective SBs are bound to increase the whole resistance of the MOSFET. Through extracting the slopes of the I-V curves by linear fitting in Figure 4(d), it is proved that the conductivity becomes smaller in the irradiated device at the same V_g and V_d. For example, the conductivity is only 7.6 S/m in the irradiated device at V_d= -40 mV and V_g= -20 V. However, the conductivity is 13.2 S/m in the same conditions in the uncapped device as shown in Figure 4(c). Furthermore, because of the increased effective drain SB for hole, clear drain current saturation was observed in the enlarged output curves. As shown in the inset of Figure 4(d), as the V_d raises to 2 V gradually, I_d almost maintains at 36 μA under the V_g = -20 V. The saturation behavior suggests that the drain SB dependent on the drain bias ($q\Phi_{Bp^*}$-qV_d) has not reached the flat-band condition as shown in Figure 5(b). Once the energy band of the BP near the drain side is approaching the flat-band as the V_d increases, the drain SB will diminish and the output curves in the large range will show saturation behavior.[76]

As the V_g keeps increasing positively, the device is dominated by the electron conductance due to the gate-induced electrostatic doping effect. Figure 4(e) displays the sublinear I-V curves in the uncapped device, which suggests that strong SBs hinder the electron injection.[77] Moreover, the highly asymmetric I-V curves illustrate that the source SB is dramatically distinct from the drain one. In the inset of Figure 4(e), typical rectifying I-V behavior without drain current saturation is observed in the large range output relationship, even when the V_g reaches 60 V. The inflection point is observed near

V_d= 0.9 V. It suggests that the height of effective SB for electron ($q\Phi_{Bn}$) in the uncapped device are extremely large to block the thermionic emission electron injection. Besides, the width of the SB is also large enough to hinder the electron tunneling current, even at a large gate bias (V_g = 60 V).[78] As shown in Figure 5(c), the high V_d (3 V) still cannot diminish the large drain SB ($q\Phi_{Bn}$-qV_d), which makes the energy bands of the BP near the drain side cannot approach the flat-band condition. Therefore, no saturation behavior is observed and the V_d is mostly loaded by the reversed SB instead of the ultrathin BP channel for the electron conductance. The degraded lateral electric field makes it difficult to reach saturation regime unless an extreme large V_d is applied.

In contrast, after the irradiation it is clearly found that the I-V curves in Figure 4(f) are more linear than those in Figure 4(e), which suggests that the effective SB for electron ($q\Phi_{Bn*}$) is reduced after the irradiation. The energy levels of the BP are dragged down by masses of electron doping as shown in Figure 5(d). The reduced effective SB can enhance the electron thermionic emission and tunneling currents, which reduces the whole resistance of the FET greatly. For instance, comparing the output curves in the inset of Figure 4(e) and (f), after the irradiation, the whole resistance of the device declines from 620 kΩ to 145 kΩ, nearly ~ 4 times in the same condition of V_g = 40 V and V_d = 100 mV. In addition, clear drain current saturation can be observed in the enlarged output curves as shown in the inset of Figure 4(f). The high V_d makes the drain SB height to decrease by $q\Phi_{Bn*}$-qV_d, which facilitates the energy band near the drain side to reach the flat-band condition and allows the hole injection from the drain electrode. However, compared with the band diagram in Figure 5(a), the reduced drain SB for electron is not as low as that for the hole current. Therefore, the drain SB is still expected to have an impact on the output curves in the electron dominated side, which makes the drain current to be saturated at high V_d (~3 V). Our explanation can be verified by the fact that the electron conductance is ~10 times smaller than the hole conductance.

Next, as the e-beam irradiation can lead to n-type doping to BP, we demonstrated a prototype of p-n diode by capping the BP channel partially with an irradiated PMMA layer and leaving the other part uncapped. The schematic diagram of the structure is shown in Figure 6(a). Figure 6(b) displays the linear and semi-logarithmic transfer curves of the p-n diode. Unlike the normal transfer curves shown in Figure 4(b), two valleys are observed in the transfer curve. Herein, we define five representative states (from A to E) to explain the transition of the energy bands in the BP p-n diode. When the V_g is much negative than -5 V (charge neutral point of the capped part), the Fermi levels of the Cr at both the source and the drain align near the E_v due to the intrinsic p-type nature of the ultrathin BP.[16] A hole accumulation layer is formed by the negative gate bias in the on-state. The larger the gate bias is, the thinner the effective SBs are. The hole thermionic and tunneling currents overcome the SBs to form large drain current. Accordingly, the I-V curves are almost linear as shown in Figure 6(c). Therefore, the p-p junction is formed in that state. As the V_g increases gradually to near -5 V, the energy bands shift downward by the electrostatic doping and the Fermi level of the BP shifts toward the conduction band. However, as the PMMA capping can induce n-type doping, the capped region of the BP channel will reach the flat-band condition in advance. An analogic i-p junction is achieved successfully. The I-V curve becomes rectified as shown in Figure 6(d). The forward bias can reduce the built-in electric field between the capped and uncapped regions. When the V_g increases over -5 V, the energy band in the capped region shifts downward further, and the Fermi level of the BP gets closer to the conduction band. Hence, the capped region has already been dominated by electron conductance. However, the uncapped region is still in hole dominated regime so that the p-n junction is formed and the built-in field between the two regions is the largest in this state. The I-V curve is rectified with the maximum rectification factor of 21.3 as shown in Figure 6(e), which is much larger than that of graphene.[79] As the V_g increases over 10 V, the uncapped region almost reaches the flat-

band condition due to the gate-induced electrostatic doping and the drain bias. The effective SB near the drain side for the electron conductance becomes lower. Large electron current passes over the SB. Oppositely, the barriers for hole starts to increase so that the whole conductance declines under the forward bias as shown in Figure 6(f). Hence, the n-i junction is formed in this condition. Finally, n-n junction is formed when the V_g increases further. Electron accumulation layer exists in the whole BP channel. Besides, the different effective SBs at the source and drain lead to the asymmetric I-V curves as shown in Figure 6(g). Based on the analysis above, it is found that the rectifying states of the BP p-n diode can be tuned by varying the V_g directly.

To investigate the influence of the partially capped and irradiated BP channel areas, we prepared three BP p-n diodes with different capped areas which are covered 25%, 50% and 75% of the whole BP channel. The results are shown in Figure 6(h). As the capped area enlarges, the number of valleys in the transfer curve changes from two to one. In addition, the charge neutral point shifts toward the negative direction more and more seriously. Moreover, the conductance in the electron dominated range becomes larger and larger gradually as the proportions of the capped area increase, which suggests that more electron dopants are introduced. The number of valleys decreases suggesting that the built-in field is quite small in the diode with the proportions of capped area larger than 25%. Therefore, with a quarter of the BP channel capped by the PMMA, the BP p-n diode can perform well enough. It is more efficient than the reported benzyl viologen solution.[46] Finally, another prototype about the logic inverter with a gain of 0.18 at V_{dd}= 1 V was also successfully demonstrated as shown in the part 3 of the supplementary information. Based on the analysis of various BP devices above, it is of great interest to utilize the PMMA capping technique to modify the electron transport properties of the ultrathin BP based devices.

3.Conclusion

In conclusion, we have comprehensively studied the influence of PMMA capping on the ultrathin BP FETs. The durability of the capped BP FETs in ambient is prolonged. It is found that the PMMA capping layer serves as an electron dopant and results in a dramatic decline of effective SB for electron injection by ~13 meV. Moreover, the capped device exhibits an enhanced on/off ratio ~7.5×10^3 for the hole conduction. After the e-beam irradiation to the PMMA layer, a larger negative shift of the charge neural point is observed, and the electron conductivities of the device are enhanced dramatically by ~4 times. As proof-of-concept device, the gate tunable p-n diode was successfully demonstrated. The rectification factor can be tuned by the gate voltage with a maximum of 21.3. Furthermore, the diode can perform well with just a quarter of the BP channel capped by the PMMA. This work demonstrates a facile and convenient method of achieving two urgent purposes simultaneously, namely, the enhanced durability in ambient and modification of the effective SB. This method of fabricating BP SB-MOSFETs with tunable effective SBs offers more opportunity to the development of 2D materials in the field of microelectronics and photonics.

4. Methods

Ultrathin BP flakes were mechanically exfoliated from commercially available nature bulk material (from Smart-Elements) using Scotch tape onto SiO_2 (285 nm)/p-type Si substrates. PMMA powder (with average Mw ca. 9.96×10^5) was dissolved in anisole solution (99.7%) for 3 days to from PMMA solution. Subsequently, the PMMA solution was spin-coated onto the substrates with the speed of 4000 rpm to form a PMMA capping layer with the thickness of ~300 nm. The substrate was heated for 5 mins at 110℃ on a hot plate to solidify the PMMA film. The experiments described above were carried out in a glove box (MBRAUN) fulfilled with argon. Optical microscope and Raman

spectroscopy (WITech alpha-300) were used to identify and characterize the BP flakes. Raman signals were acquired from the same spot in the whole processes to enhance the comparability. The laser power (488 nm) was set as 0.5 mW to prevent the heating damage to the BP flakes. The capped BP flake was transferred into a vacuum chamber for electron beam lithography to pattern the source and drain electrodes. After dipping into the developer, the sample was immediately transferred into the vacuum chamber of the electron beam evaporator, a layer of 5 nm/60 nm Cr/Au was deposited as the source and drain metal under the base vacuum of 10^{-7} Torr. The evaporation rates for Cr and Au were set as 0.3 Å/s and 0.7 Å/s, respectively. Subsequently, the standard lift-off processes were carried out to pattern the contact electrodes. To enhance the contact electric properties, the device was rapidly annealed in argon ambient at 300 ℃ for 10 minutes. To selectively cover the BP FET, we utilized the e-beam irradiation. Specifically, a PMMA layer was spin-coated onto the as-fabricated BP FET with the speed of 4000 rpm. After soft baking at 110℃ for 1 min, the e-beam lithography technique was employed to selectively expose the PMMA with a high dose of 2×10^4 μC/cm^2. The filament voltage was configured as 25 keV. The PMMA in the exposed area was solidified. Subsequently, acetone was used to remove the non-irradiated PMMA. For the BP p-n diode, through the irradiation to the PMMA layer, we capped a part of the BP channel with the PMMA layer and left the other part uncapped. All the electrical measurements were carried out using Keithley 4200 in a vacuum chamber of 10^{-6} Torr at room temperature. A Desi-vac container was employed to transfer sample between each step.

Acknowledgements

YYL and SHL contributed equally to this work. This work was financially supported by the PolyU grants (1-ZVGH and 1-BBAD) and the Research Grants Council of Hong Kong (Project no. PolyU 153271/16P).

Conflict of Interest

The authors declare no conflict of interest.

References

[1] Akahama Y, Endo S and Narita S i 1983 Electrical Properties of Black Phosphorus Single Crystals *J. Phys. Soc. Jpn.* **52** 2148-2155

[2] Qiao J, Kong X, Hu Z X, Yang F and Ji W 2014 High-Mobility Transport Anisotropy and Linear Dichroism in Few-Layer Black Phosphorus *Nat. Commun.* **5** 4475

[3] Churchill H O and Jarillo Herrero P 2014 Two-Dimensional Crystals: Phosphorus Joins the Family *Nat. Nanotechnol.* **9** 330-331

[4] Li L, Yu Y, Ye G J, Ge Q, Ou X, Wu H, Feng D, Chen X H and Zhang Y 2014 Black Phosphorus Field-Effect Transistors *Nat. Nanotechnol.* **9** 372-377

[5] Xia F, Wang H and Jia Y 2014 Rediscovering Black Phosphorus as an Anisotropic Layered Material for Optoelectronics and Electronics *Nat. Commun.* **5** 4458

[6] Li Y Y, Hu Z X, Lin S H, Lai S K, Ji W and Lau S P 2017 Giant Anisotropic Raman Response of Encapsulated Ultrathin Black Phosphorus by Uniaxial Strain *Adv. Func. Mater.* **27** 1600986

[7] Chen H, Huang P, Guo D and Xie G 2016 Anisotropic Mechanical Properties of Black Phosphorus Nanoribbons *J. Phys. Chem. C* **120** 29491-29497

[8] Wang X, Jones A M, Seyler K L, Tran V, Jia Y, Zhao H, Wang H, Yang L, Xu X and Xia F 2015 Highly Anisotropic and Robust Excitons in Monolayer Black Phosphorus *Nat. Nanotechnol.* **10** 517-521

[9] Fei R, Faghaninia A, Soklaski R, Yan J A, Lo C and Yang L 2014 Enhanced Thermoelectric Efficiency via Orthogonal Electrical and Thermal Conductances in Phosphorene *Nano Lett* **14** 6393-9

[10] Buscema M, Groenendijk D J, Blanter S I, Steele G A, van der Zant H S and Castellanos Gomez A 2014 Fast and broadband photoresponse of few-layer black phosphorus field-effect transistors *Nano Lett.* **14** 3347-52

[11] Low T, Engel M, Steiner M and Avouris P 2014 Origin of photoresponse in black phosphorus phototransistors *Phys. Rev. B* **90**

[12] Sun J, Zheng G, Lee H-W, Liu N, Wang H, Yao H, Yang W and Cui Y 2014 Formation of Stable Phosphorus–Carbon Bond for Enhanced Performance in Black Phosphorus Nanoparticle–Graphite Composite Battery Anodes *Nano Lett.* **14** 4573-4580

[13] Kou L, Frauenheim T and Chen C 2014 Phosphorene as a Superior Gas Sensor: Selective

Adsorption and DistinctI–VResponse *J. Phys. Chem. Lett.* **5** 2675-2681

[14] Du Y, Liu H, Deng Y and Ye P D 2014 Device Perspective for Black Phosphorus Field-Effect Transistors: Contact Resistance, Ambipolar Behavior, and Scaling *ACS Nano* **8** 10035-10042

[15] Castellanos-Gomez A, Vicarelli L, Prada E, Island J O, Narasimha-Acharya K L, Blanter S I, Groenendijk D J, Buscema M, Steele G A, Alvarez J V, Zandbergen H W, Palacios J J and van der Zant H S J 2014 Isolation and characterization of few-layer black phosphorus *2D Mater.* **1** 025001

[16] Koenig S P, Doganov R A, Schmidt H, Castro Neto A H and Özyilmaz B 2014 Electric field effect in ultrathin black phosphorus *Appl. Phys. Lett.* **104** 103106

[17] Joshua O I, Gary A S, Herre S J v d Z and Andres C-G 2015 Environmental instability of few-layer black phosphorus *2D Mater.* **2** 011002

[18] Gamage S, Li Z, Yakovlev V S, Lewis C, Wang H, Cronin S B and Abate Y 2016 Nanoscopy of Black Phosphorus Degradation *Advanced Materials Interfaces* **3** 1600121

[19] Ma X, Lu W, Chen B, Zhong D, Huang L, Dong L, Jin C and Zhang Z 2015 Performance change of few layer black phosphorus transistors in ambient *AIP Advances* **5** 107112

[20] Huang Y, Qiao J, He K, Bliznakov S, Sutter E, Chen X, Luo D, Meng F, Su D, Decker J, Ji W, Ruoff R S and Sutter P 2016 Interaction of Black Phosphorus with Oxygen and Water *Chemistry of Materials* **28** 8330

[21] Wood J D, Wells S A, Jariwala D, Chen K S, Cho E, Sangwan V K, Liu X, Lauhon L J, Marks T J and Hersam M C 2014 Effective Passivation of Exfoliated Black Phosphorus Transistors against Ambient Degradation *Nano Lett.* **14** 6964

[22] Kim J S, Liu Y, Zhu W, Kim S, Wu D, Tao L, Dodabalapur A, Lai K and Akinwande D 2015 Toward air stable multilayer phosphorene thin films and transistors *Sci. Rep.* **5** 8989

[23] Illarionov Y Y, Waltl M, Rzepa G, Kim J S, Kim S, Dodabalapur A, Akinwande D and Grasser T 2016 Long-Term Stability and Reliability of Black Phosphorus Field-Effect Transistors *ACS Nano* **10** 9543

[24] Bensong W, Bingchao Y, Yue W, Junying Z, Zhongming Z, Zhongyuan L and Wenhong W 2015 Enhanced stability of black phosphorus field-effect transistors with SiO 2 passivation *Nanotechnology* **26** 435702

[25] Sinha S, Takabayashi Y, Shinohara H and Kitaura R 2016 Simple fabrication of air-stable black phosphorus heterostructures with large-area hBN sheets grown by chemical vapor deposition method

2D Mater. **3** 035010

[26] Avsar A, Vera-Marun I J, Tan J Y, Watanabe K, Taniguchi T, Castro Neto A H and Özyilmaz B 2015 Air-Stable Transport in Graphene-Contacted, Fully Encapsulated Ultrathin Black Phosphorus-Based Field-Effect Transistors *ACS Nano* **9** 4138-4145

[27] Doganov R A, O'Farrell E C, Koenig S P, Yeo Y, Ziletti A, Carvalho A, Campbell D K, Coker D F, Watanabe K, Taniguchi T, Castro Neto A H and Ozyilmaz B 2015 Transport properties of pristine few-layer black phosphorus by van der Waals passivation in an inert atmosphere *Nat. Commun.* **6** 6647

[28] Tayari V, Hemsworth N, Fakih I, Favron A, Gaufres E, Gervais G, Martel R and Szkopek T 2015 Two-dimensional magnetotransport in a black phosphorus naked quantum well *Nat. Commun.* **6** 7702

[29] Favron A, Gaufres E, Fossard F, Phaneuf-Lheureux A-L, Tang N Y W, Levesque P L, Loiseau A, Leonelli R, Francoeur S and Martel R 2015 Photooxidation and quantum confinement effects in exfoliated black phosphorus *Nat Mater* **14** 826-832

[30] Zhao Y, Wang H, Huang H, Xiao Q, Xu Y, Guo Z, Xie H, Shao J, Sun Z, Han W, Yu X F, Li P and Chu P K 2016 Surface Coordination of Black Phosphorus for Robust Air and Water Stability *Angewandte Chemie* **55** 5003-7

[31] Ryder C R, Wood J D, Wells S A, Yang Y, Jariwala D, Marks T J, Schatz G C and Hersam M C 2016 Covalent functionalization and passivation of exfoliated black phosphorus via aryl diazonium chemistry *Nat Chem* **8** 597-602

[32] Yue D, Lee D, Jang Y D, Choi M S, Nam H J, Jung D Y and Yoo W J 2016 Passivated ambipolar black phosphorus transistors *Nanoscale* **8** 12773-9

[33] Liu H, Neal A T and Ye P D 2012 Channel Length Scaling of MoS2 MOSFETs *ACS Nano* **6** 8563-8569

[34] Suh J, Park T E, Lin D Y, Fu D, Park J, Jung H J, Chen Y, Ko C, Jang C, Sun Y, Sinclair R, Chang J, Tongay S and Wu J 2014 Doping against the native propensity of MoS2: degenerate hole doping by cation substitution *Nano Lett* **14** 6976-82

[35] Nipane A, Karmakar D, Kaushik N, Karande S and Lodha S 2016 Few-Layer MoS_2 p-Type Devices Enabled by Selective Doping Using Low Energy Phosphorus Implantation *ACS Nano* **10** 2128-37

[36] Yu Y-J, Zhao Y, Ryu S, Brus L E, Kim K S and Kim P 2009 Tuning the Graphene Work Function

by Electric Field Effect *Nano Lett.* **9** 3430-3434

[37] Lu C-P, Li G, Mao J, Wang L-M and Andrei E Y 2014 Bandgap, Mid-Gap States, and Gating Effects in MoS2 *Nano Lett.* **14** 4628-4633

[38] Schulman D S, Arnold A J and Das S 2018 Contact engineering for 2D materials and devices *Chem. Soc. Rev.* **47** 3037-3058

[39] Schmidt H, Giustiniano F and Eda G 2015 Electronic transport properties of transition metal dichalcogenide field-effect devices: surface and interface effects *Chem. Soc. Rev.* **44** 7715-7736

[40] Li L, Engel M, Farmer D B, Han S J and Wong H P 2016 High-Performance p-Type Black Phosphorus Transistor with Scandium Contact *ACS Nano* **10** 4672

[41] Wang C H, Incorvia J A C, McClellan C J, Yu A C, Mleczko M J, Pop E and Wong H P 2018 Unipolar n-Type Black Phosphorus Transistors with Low Work Function Contacts *Nano Lett*

[42] Koenig S P, Doganov R A, Seixas L, Carvalho A, Tan J Y, Watanabe K, Taniguchi T, Yakovlev N, Castro Neto A H and Ozyilmaz B 2016 Electron Doping of Ultrathin Black Phosphorus with Cu Adatoms *Nano Lett* **16** 2145-51

[43] Pan Y, Wang Y, Ye M, Quhe R, Zhong H, Song Z, Peng X, Yu D, Yang J, Shi J and Lu J 2016 Monolayer Phosphorene–Metal Contacts *Chemistry of Materials* **28** 2100-2109

[44] Xu Y, Yuan J, Zhang K, Hou Y, Sun Q, Yao Y, Li S, Bao Q, Zhang H and Zhang Y 2017 Field-Induced n-Doping of Black Phosphorus for CMOS Compatible 2D Logic Electronics with High Electron Mobility *Adv. Func. Mater.* **27** 1702211

[45] Xiang D, Han C, Wu J, Zhong S, Liu Y, Lin J, Zhang X A, Ping Hu W, Ozyilmaz B, Neto A H, Wee A T and Chen W 2015 Surface transfer doping induced effective modulation on ambipolar characteristics of few-layer black phosphorus *Nat. Commun.* **6** 6485

[46] Yu X, Zhang S, Zeng H and Wang Q J 2016 Lateral black phosphorene P–N junctions formed via chemical doping for high performance near-infrared photodetector *Nano Energy* **25** 34-41

[47] Liu H, Neal A T, Si M, Du Y and Ye P D 2014 The Effect of Dielectric Capping on Few-Layer Phosphorene Transistors: Tuning the Schottky Barrier Heights *IEEE Electron Device Letters* **35** 795-797

[48] Han C, Hu Z, Gomes L C, Bao Y, Carvalho A, Tan S J R, Lei B, Xiang D, Wu J, Qi D, Wang L, Huo F, Huang W, Loh K P and Chen W 2017 Surface Functionalization of Black Phosphorus via Potassium toward High-Performance Complementary Devices *Nano Lett* **17** 4122-4129

[49] Wang G, Bao L, Pei T, Ma R, Zhang Y Y, Sun L, Zhang G, Yang H, Li J, Gu C, Du S, Pantelides S T, Schrimpf R D and Gao H J 2016 Introduction of Interfacial Charges to Black Phosphorus for a Family of Planar Devices *Nano Lett* **16** 6870

[50] Das S, Zhang W, Demarteau M, Hoffmann A, Dubey M and Roelofs A 2014 Tunable Transport Gap in Phosphorene *Nano Lett.* **14** 5733

[51] Das S, Demarteau M and Roelofs A 2014 Ambipolar Phosphorene Field Effect Transistor *ACS Nano* **8** 11730-11738

[52] Zhang Z, Yao K, Liu Y, Jin C, Liang X, Chen Q and Peng L M 2007 Quantitative Analysis of Current–Voltage Characteristics of Semiconducting Nanowires: Decoupling of Contact Effects *Adv. Func. Mater.* **17** 2478

[53] Ling X, Liang L, Huang S, Puretzky A A, Geohegan D B, Sumpter B G, Kong J, Meunier V and Dresselhaus M S 2015 Low-Frequency Interlayer Breathing Modes in Few-Layer Black Phosphorus *Nano Lett.* **15** 4080-4088

[54] Sugai S, Ueda T and Murase K 1981 Pressure Dependence of the Lattice Vibration in the Orthorhombic and Rhombohedral Structures of Black Phosphorus *J. Phys. Soc. Jpn.* **50** 3356-3361

[55] Li Q, Chen J, Feng Z, Feng L, Yao D and Wang S 2016 The Role of Air Adsorption in Inverted Ultrathin Black Phosphorus Field-Effect Transistors *Nanoscale Res. Lett.* **11** 521

[56] Du H, Lin X, Xu Z and Chu D 2015 Recent developments in black phosphorus transistors *Journal of Materials Chemistry C* **3** 8760-8775

[57] Jiménez D, Cartoixà X, Miranda E, Suñé J, Chaves F A and Roche S 2007 A simple drain current model for Schottky-barrier carbon nanotube field effect transistors *Nanotechnology* **18** 025201

[58] Farmer D B, Golizadeh-Mojarad R, Perebeinos V, Lin Y M, Tulevski G S, Tsang J C and Avouris P 2009 Chemical doping and electron-hole conduction asymmetry in graphene devices *Nano Lett* **9** 388-92

[59] Schmidt H, Giustiniano F and Eda G 2015 Electronic transport properties of transition metal dichalcogenide field-effect devices: surface and interface effects *Chem. Soc. Rev.* **44** 7715-36

[60] Schedin F, Geim A K, Morozov S V, Hill E W, Blake P, Katsnelson M I and Novoselov K S 2007 Detection of individual gas molecules adsorbed on graphene *Nat Mater* **6** 652-5

[61] Perera M M, Lin M-W, Chuang H-J, Chamlagain B P, Wang C, Tan X, Cheng M M-C, Tománek D and Zhou Z 2013 Improved Carrier Mobility in Few-Layer MoS2 Field-Effect Transistors with

Ionic-Liquid Gating *ACS Nano* **7** 4449-4458

[62] Kenji K, Tetsuya T and Toshihiko K 2007 Modulation of CoSi 2 /Si Schottky Barrier Height by Charge Transfer Doping Utilizing Cesium Segregation at the SiO 2 /Si Interface *Jap. J. Appl. Phys.* **46** L110

[63] Zhang X, Shao Z, Zhang X, He Y and Jie J 2016 Surface Charge Transfer Doping of Low-Dimensional Nanostructures toward High-Performance Nanodevices *Adv. Mater.* **28** 10409-10442

[64] Chen Y-F and Fuhrer M S 2006 Tuning from Thermionic Emission to Ohmic Tunnel Contacts via Doping in Schottky-Barrier Nanotube Transistors *Nano Lett.* **6** 2158-2162

[65] Allain A, Kang J, Banerjee K and Kis A 2015 Electrical contacts to two-dimensional semiconductors *Nature Mater.* **14** 1195

[66] Allain A, Kang J, Banerjee K and Kis A 2015 Electrical contacts to two-dimensional semiconductors *Nature Mater.* **14** 1195-205

[67] Penumatcha A V, Salazar R B and Appenzeller J 2015 Analysing black phosphorus transistors using an analytic Schottky barrier MOSFET model *Nat. Commun.* **6** 8948

[68] Das S, Demarteau M and Roelofs A 2014 Ambipolar phosphorene field effect transistor *ACS Nano* **8** 11730

[69] Du Y, Yang L, Zhou H and Ye P D 2016 Performance Enhancement of Black Phosphorus Field-Effect Transistors by Chemical Doping *IEEE Electron Device Letters* **37** 429-432

[70] Liu Y, Guo J, Zhu E, Liao L, Lee S J, Ding M, Shakir I, Gambin V, Huang Y and Duan X 2018 Approaching the Schottky-Mott limit in van der Waals metal-semiconductor junctions *Nature* **557** 696-700

[71] Prakash A, Ilatikhameneh H, Wu P and Appenzeller J 2017 Understanding contact gating in Schottky barrier transistors from 2D channels *Sci. Rep.* **7** 12596

[72] Das S, Chen H Y, Penumatcha A V and Appenzeller J 2013 High performance multilayer MoS_2 transistors with scandium contacts *Nano Lett.* **13** 100

[73] Li X, Grassi R, Li S, Li T, Xiong X, Low T and Wu Y 2018 Anomalous Temperature Dependence in Metal-Black Phosphorus Contact *Nano Lett.* **18** 26

[74] Deng B, Tran V, Xie Y, Jiang H, Li C, Guo Q, Wang X, Tian H, Koester S J, Wang H, Cha J J, Xia Q, Yang L and Xia F 2017 Efficient electrical control of thin-film black phosphorus bandgap *Nat. Commun.* **8** 14474

[75] Lee E H, Rao G R and Mansur L K 1999 LET effect on cross-linking and scission mechanisms of PMMA during irradiation *Radiation Physics and Chemistry* **55** 293-305

[76] Liu H, Si M, Deng Y, Neal A T, Du Y, Najmaei S, Ajayan P M, Lou J and Ye P D 2013 Switching mechanism in single layer MoS2 transistors an insight into current flow across Schottky barriers *ACS Nano* **8** 1031

[77] Zhang Z, Yao K, Liu Y, Jin C, Liang X, Chen Q and Peng L M 2007 Quantitative Analysis of Current–Voltage Characteristics of Semiconducting Nanowires: Decoupling of Contact Effects *Adv. Func. Mater.* **17** 2478-2489

[78] Javey A, Guo J, Wang Q, Lundstrom M and Dai H 2003 Ballistic carbon nanotube field-effect transistors *Nature* **424** 654

[79] Kim S, Shin D H, Kim C O, Kang S S, Kim J M, Jang C W, Joo S S, Lee J S, Kim J H, Choi S-H and Hwang E 2013 Graphene p–n Vertical Tunneling Diodes *ACS Nano* **7** 5168-5174

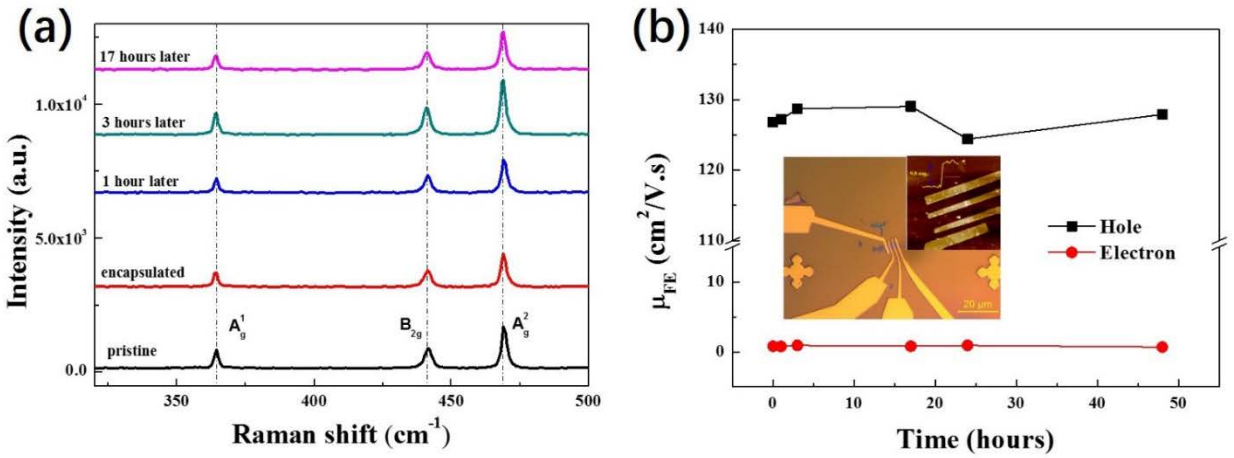

Figure 1. The influence of PMMA capping on the durability of BP SB-MOSFET stored in ambient. a) Raman spectra of the capped ultrathin BP flake as a function of the storage time in ambient. Notably, the black one in the bottom represents the Raman spectrum of the uncapped ultrathin BP flake. b) The dependence of electron and hole mobilities on the storage time for the capped FET. The insets are the optical image and the AFM image of the device. The height of this ultrathin BP flake is ~9.8 nm. The channel length of the BP FET is 4.6 μm, and the width of 2.8 μm.

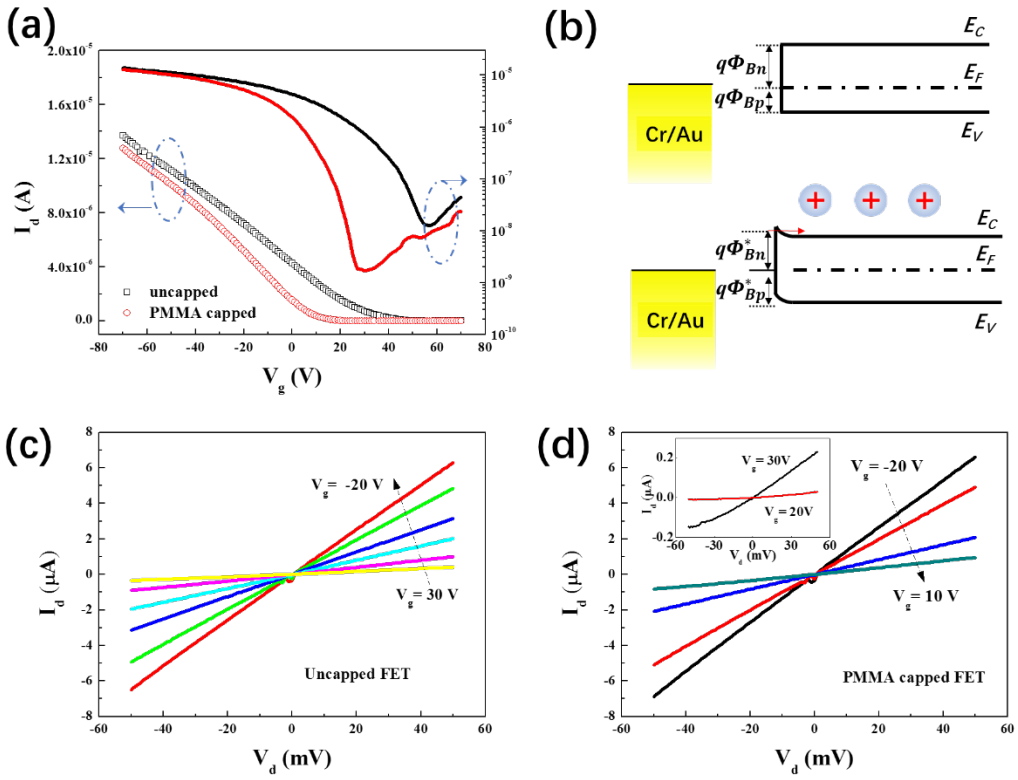

Figure 2. The influence of PMMA capping on the electrical transport properties of BP SB-MOSFET with channel length of 1.7 μm and width of 4.0 μm. a) Linear and semi-logarithmic plots of transfer curves of the FET before (black one) and after (red one) the capping. The source-drain voltage (V_d) was set as 100 mV. b) The schematic diagrams of the energy bands of the uncapped BP (upper panel) and the capped one (lower panel). E_V, E_F and E_c represent the valence band, Fermi level and the conductive band, respectively. $q\Phi_{Bn}$ and $q\Phi_{Bp}$ represent the effective SBs for electron and hole in the uncapped FET, respectively. $q\Phi^*_{Bn}$ and $q\Phi^*_{Bp}$ are the effective SBs in the capped FET. c) I-V curves of the uncapped FET under the gate voltage (V_g) from -20 V to 30 V with a step of 10 V. d) I-V curves of the same FET with the capping layer under V_g from -20 V to 10 V with a step of 10 V. The inset shows the I-V curves under V_g = 20 V and 30 V, respectively.

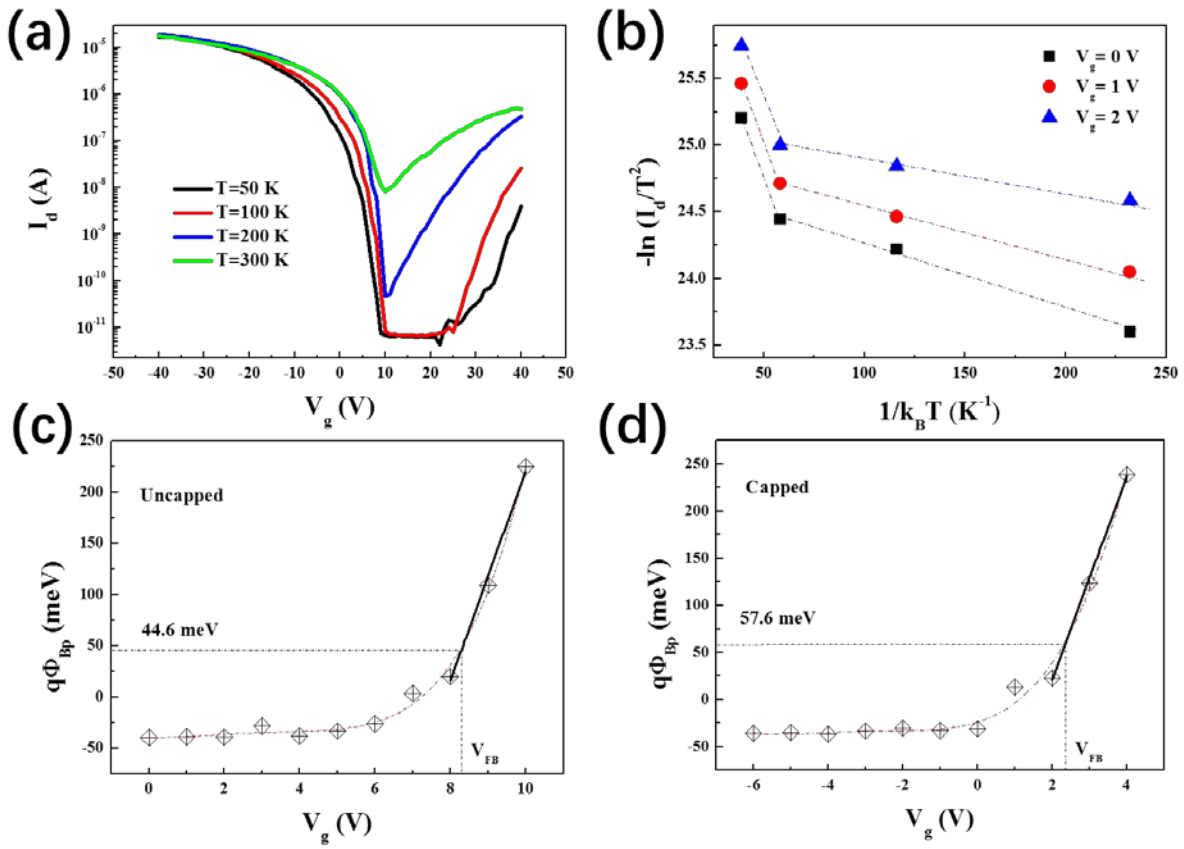

Figure 3. The extraction of effective SB in BP SB-MOSFET with the channel length of 2.0 μm and width of 3.7 μm. a) Experimental transfer characteristics of the uncapped FET with Cr/Au contacts under different operating temperatures. b) Arrhenius-type plot composed of the -ln (I_d/T^2) as a function of the 1/k_BT at different gate voltages. c-d) The extracted effective SB for hole conduction ($q\Phi_{Bp}$) as a function of the applied gate voltages in the uncapped BP FET (c) and capped BP FET (d), respectively.

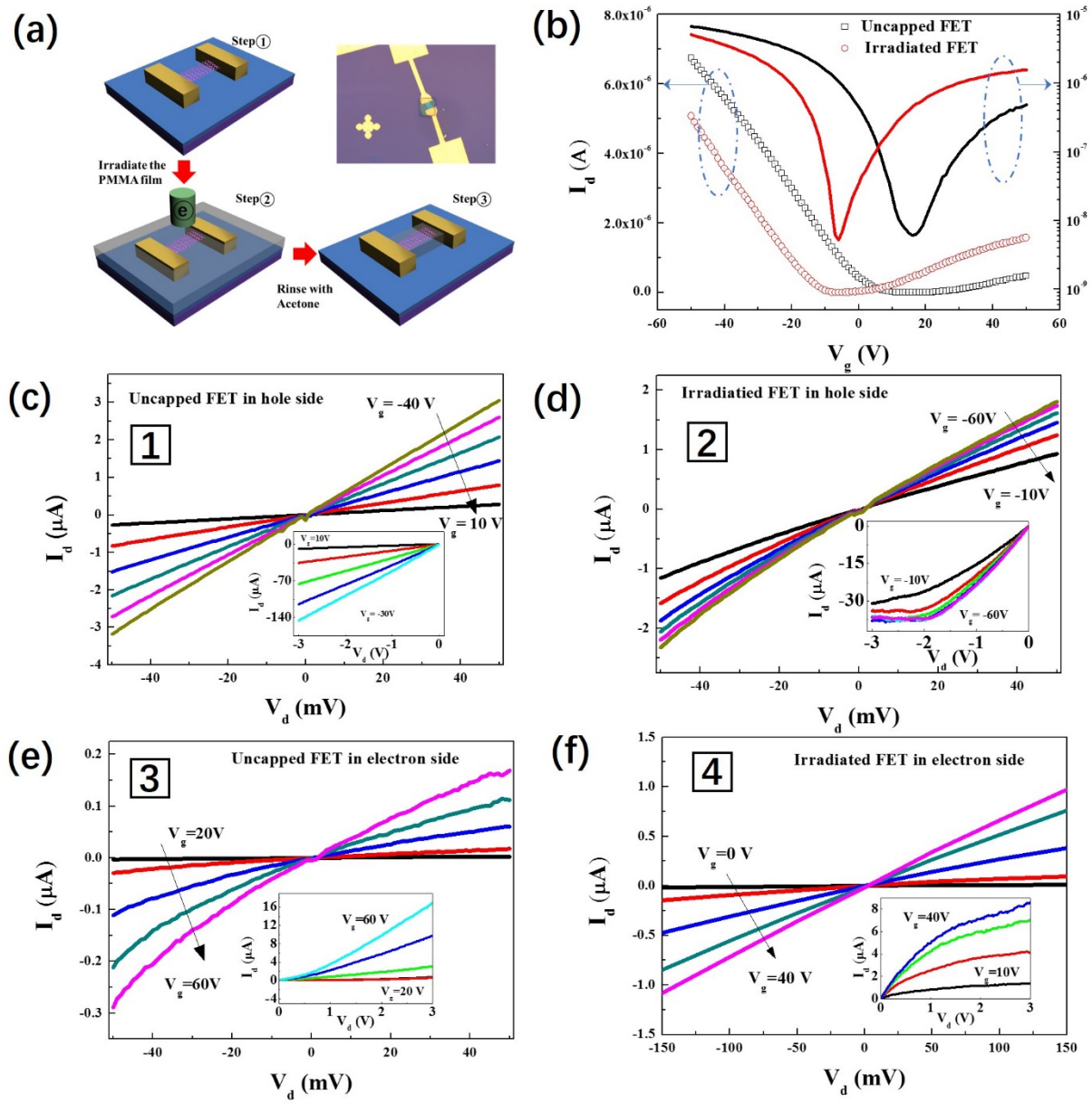

Figure 4. The influence of the irradiation to PMMA layer on the electrical transport properties of BP SB-MOSFET with the channel length of 4.8 μm and width of 3.0 μm. a) The schematic diagrams of the process of the irradiation. In step 1, an as-fabricated FET was spin-coated with a layer of PMMA. In step 2, the PMMA layer was exposed by e-beam irradiation. In step 3, the non-irradiated PMMA was rinsed away by acetone with the exposed area left. The photo of the final device is also displayed in the upper right corner. b) Linear and semi-logarithmic plots of transfer characteristics of the FET before (black lines) and after (red lines) the irradiation. c) I-V curves of the uncapped FET in the

small range of V_d in hole dominated side. V_g varies from -40 V to 10 V. The inset shows the corresponding hole dominated output curves in the enlarged range. V_g changes from -30 V to 10 V. d) I-V curves of the irradiated FET in the small range of V_d in hole dominated side. V_g changes from -60 V to -10 V. The inset shows the corresponding hole dominated output curves in the enlarged range. e) I-V curves of the uncapped FET in the small range of V_d in electron dominated side. V_g changes from 20 V to 60 V. The inset shows the corresponding electron dominated output curves in the enlarged range. f) I-V curves of the irradiated FET in the small range of V_d in the electron dominated side. V_g changes from 10 V to 60 V. The inset shows the corresponding electron dominated curves in the enlarged range.

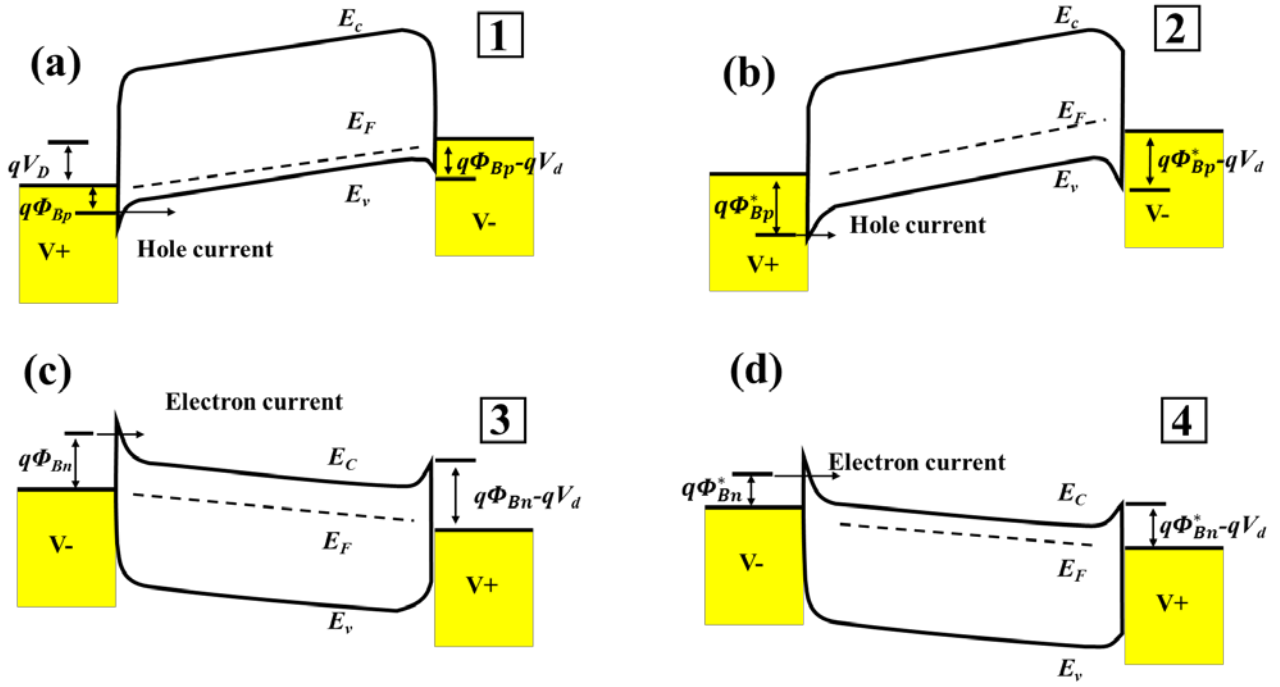

Figure 5. Qualitative energy band diagrams of the BP SB-MOSFET. Schematic diagrams of the energy band structures between the BP and metal contacts before a) and after b) the irradiation in the hole dominated side. Analogously, the energy band structures before c) and after d) the irradiation in the electron dominated side. The numbers (1-4) in the four panels are corresponding to the I-V curves shown in Figure 4(c-f). E_c and E_v represent the minimum energy of the conductive band the maximum energy of the valence band, respectively. E_F is the Fermi level energy. $q\Phi_{Bn}$ and $q\Phi_{Bp}$ represent the effective SBs for electron and hole in the uncapped device, respectively. $q\Phi^*_{Bn}$ and $q\Phi^*_{Bp}$ represent the effective SBs for the electron and hole in the irradiated device, respectively. The potential difference between the source and the drain is V_d.

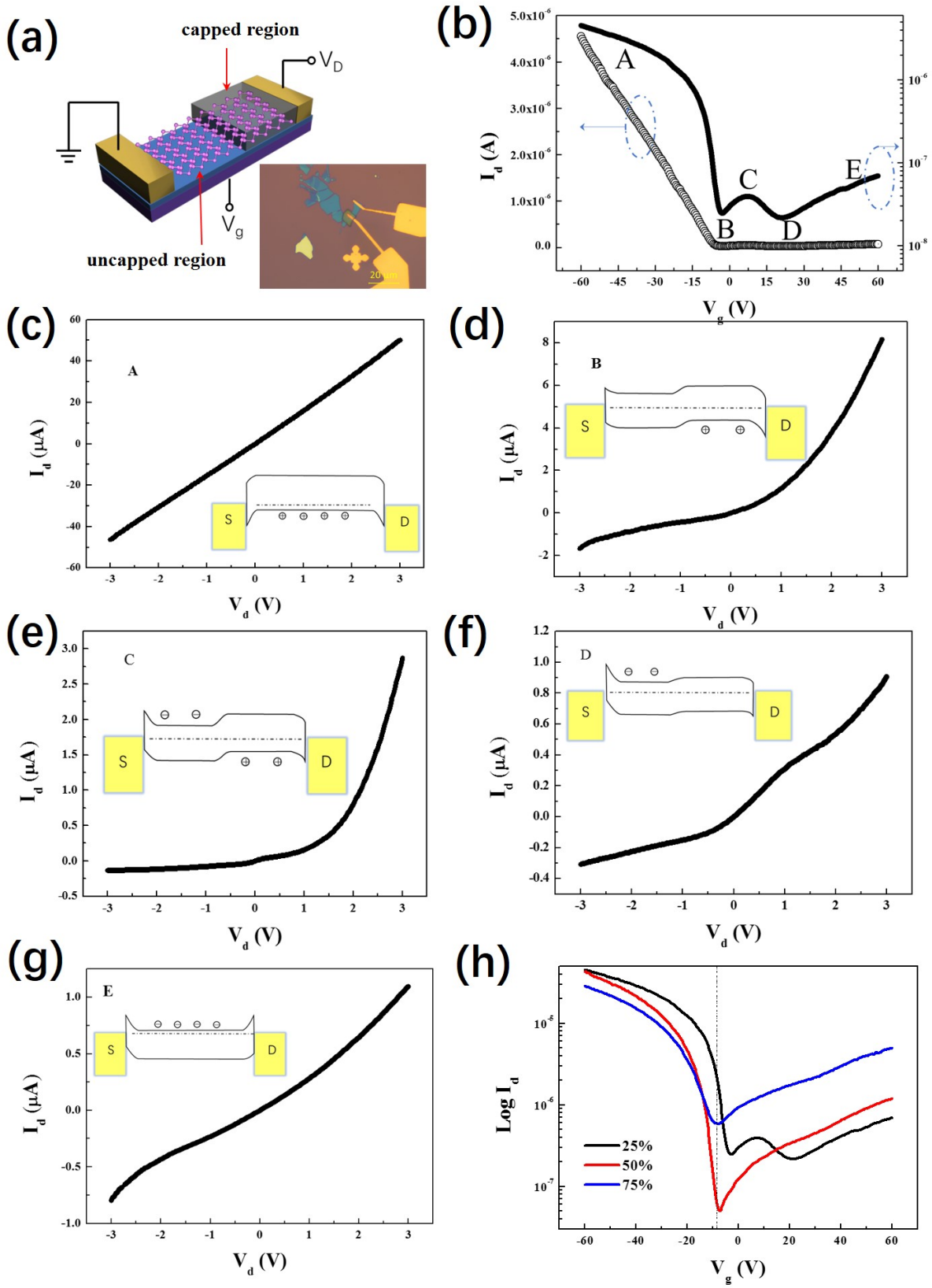

Figure.6 Electrical properties of BP p-n diode with Cr/Au metal stacks as contact electrodes. The whole channel length is 7.5 μm and the width of the channel is 3.0 μm. a) The schematic diagram and

photo of the BP p-n diode fabricated by selectively capping part of the BP channel through the e-beam irradiation. b) Linear and semi-logarithmic plots of the transfer curves of the BP p-n diode. Five main states are labeled as A to F, respectively. c-g) Corresponding I-V curves under the five states. The insets show the corresponding band diagrams at each stage. h) Transfer curves for the BP p-n diode with different proportions of the capped areas for the whole BP channel.